

Wake Formation Flow Physics and Boundary Layer Analysis on the Sides of the Isosceles Triangular Cylinder with Apex Pointing Downstream

Namit Agrawal

Department of Mechanical Engineering,
Graphic Era Deemed to be University, Dehradun, Uttarakhand, India.
Corresponding author: agrawalnमित@gmail.com

Ritvik Dobriyal

Department of Mechanical Engineering,
Graphic Era Deemed to be University, Dehradun, Uttarakhand, India.
E-mail: ritvikdobriyal@geu.ac.in

Maharshi Subhash

Phimach Institute of Learning and Advanced Research, Dhanbad, Jharkhand, India.
E-mail: phimachinstitute@gmail.com

(Received on October 1, 2023; Revised on December 10, 2023 & January 13, 2024; Accepted on January 18, 2024)

Abstract

Boundary layer interaction with downstream flow structures was numerically studied to find the region of inactivity behind an 75° isosceles triangular cylinder with apex pointing downstream at intermediate Reynolds numbers ($Re = 520, 640, 840$ and 1040). The Standard $k-\epsilon$ model in OpenFOAM was used in the study. Numerical results were validated against Particle Image Velocimetry data. Results revealed the stable region of inactivity characterized by low turbulent kinetic energy and vorticity. The onset of secondary vortex and separation point, independent of Reynolds number, was identified. The onset of the secondary vortex was located at ($x = 2 \text{ mm}$) from the base and ($y = 1.5 \text{ mm}$) from the apex on either side of the cylinder. The ratio of modulus of absolute primary z -component of vorticity, $|\omega_z^1|$, to the modulus of secondary z -component of vorticity, $|\omega_z^2|$, was found to be approximately equal to 1.2. This ratio is invariant of the Reynolds number of the study. These findings have practical implications. The unique properties of the inactivity region forms an ideal location that can be used for injecting fluid, placing measurement probe, active flow control and drag reduction. The research problem is formulated in the introduction. Literature is reviewed next providing the background. Details about the range of parameters, governing equations, numerical study details and software used are given in the methodology section. The results section gives the numerical results, verified by mesh refinement test and validated against experimental results. The results are finally discussed in the next section.

Keywords- Boundary layer, Inactivity region, Primary vortex, Secondary vortex, Intermediate Reynolds number.

1. Introduction

The boundary layer plays a significant role in the behavior of flow around solid objects. The fluid's viscosity interacts with the velocity gradient near the solid surface. This interaction results in the formation of the boundary layer. As the fluid (like air or water) flows over the object's surface, it sticks to the surface due to viscosity. The fluid sticks to the surface in the form of a thin fluid layer known as the boundary layer. The boundary layers affect flow parameters like drag, lift and heat transfer. The physics behind the formation of a boundary layer has many practical applications. This study is beneficial to applications like boundary layer control techniques.

The sharp-edged bluff body is one such practical application. The physics behind boundary layer development is different for different bluff bodies. For example, the triangular cylinder with apex pointing downstream (DOWN) configuration is an interesting avenue to be explored. Because the

boundary layer develops after the separation of free shear layers. Moreover, this boundary layer interacts with the flow structure downstream. This interaction has several potential practical applications. On the contrary, the flow over a triangular cylinder with apex pointing upstream (UP) configuration is different. Here the boundary layer is developed first. Then the edges separate the boundary layer as free shear layers.

El-Sherbiny (1983) investigated a 90° triangular cylinder in DOWN configuration. The study focused on pressure distribution on the sides of the cylinder. The observed pressure distribution patterns showed how the flow interacts with the cylinder's surface. The study also showed the influence of flow on the behaviour of the boundary layer. However, the study provided limited insights into boundary layer behavior. In an experimental study, Nakagawa (1989) discussed the influence of boundary layer on free shear layers formed around triangular cylinder in DOWN configuration. The study focussed only on the effect of boundary layer thickness and separation characteristics on separated shear layers. El Wahed et al. (1993) focused on the flow around triangular cylinders DOWN configuration. The study showed the presence of recirculation zones and provided an understanding of symmetry. These observations provided insights into boundary layer separation and reattachment on the sides of the cylinder. Iungo and Buresti (2009) stated that varying the aspect ratio may affect the boundary layer. This variation further affects the boundary layer interaction with the cylinder's sides. The data infers that the thickness and dynamics of the boundary layer play an important role. These two factors determine drag coefficients and flow interaction with the cylinder's surface. These four studies suggest the importance of the understanding of the behaviour of the boundary layer. The boundary layer behaviour is crucial for the understanding of the fluid dynamics and performance optimisation of triangular cylinders.

There exists a complex interplay between the wake behaviour, vortex shedding patterns and the boundary layer around triangular cylinders. This complex interplay has been examined in multiple investigations both experimental and numerical in nature. For example, multiple studies were undertaken out by Iungo and Buresti (2003), Buresti and Iungo (2008), Buresti and Iungo (2010) and further carried by Iungo and Lombardi (2011). The authors emphasised wake characteristics and vortex shedding. These studies indicated the likely effect of the boundary layer on the wake dynamics. Similar studies were undertaken by Ozgoren et al. (2015) and Yagmur et al. (2017). The authors suggested the potential influence of the boundary layer on flow patterns and vortex shedding. Other studies undertaken by Mahato et al. (2018) and Seyed-Aghazadeh et al. (2017) focussed on vortex shedding and flow dynamics. These studies implied that the boundary layer and vortex shedding behaviour are connected. The role of boundary layer in shaping wake dynamics, vortex shedding patterns and flow behaviour around triangular cylinder has been highlighted in these studies.

Cheng and Liu (2000) and Wang et al. (2019b) considered the interaction of the boundary layer with free shear layers crucial. They found that the flow interacts with the boundary layer as it circulates on the sides of the cylinder. This interaction can influence the separation of shear layers from the surface. Moreover, this interaction can affect the conditions that induce vortex shedding. Hence, affecting the frequency and characteristics of vortex shedding. Tu et al. (2014) and Ng et al. (2016) focused on the characteristics of vortex shedding and flow separation patterns. The authors observed the boundary layer as it interacted with the sides of the cylinder. The influence of boundary layer on flow separation and vortex shedding was observed. The interaction of boundary layer with the separated shear layers cause shedding patterns. These shedding patterns affect the wake structure and flow dynamics. In a numerical study, Jusoh et al. (2020) examined orientation effects on the flow structure. Increased drag coefficients and wake size with increase in apex angle were shown. The results were consistent with published literature. These studies show how the boundary layer affect separation, shear layer and wake. Yet, there is no explicit discussion

on the boundary layer. Knowing how the boundary layer interacts with vortex shedding is crucial to understanding the dynamics of the flow.

Djebedjian (2002), Camarri et al. (2006), Rui et al. (2019), Derakhshandeh and Alam (2019) and Feshalami et al. (2022) studied wake features, vorticity and flow variations in bluff bodies. These studies examined the relationship between wake behavior and boundary layer interaction. However, these studies do not explicitly address the boundary layer.

Numerical studies focusing on apex pointing upstream, shed light on the intricate interplay between the boundary layer and wake behaviour around triangular cylinders. For instance, Luo et al. (1994) explored the impact of various cross-sectional shapes and found that the triangular cylinder with apex pointing upstream exhibited the least interaction between separated shear layers and side faces. Similarly, in a numerical study conducted by Prasath et al. (2014) analysed wake characteristics, revealing correlations between wake bubble length, Reynolds number (Re), and aspect ratios. While not explicitly discussing the boundary layer, these studies do provide insights into how wake patterns and dynamics are influenced by the boundary layer. In another numerical study Wang et al. (2019a) conducted on four cylinders with different cross-sectional shapes to examine their impact on flow field characteristics, showed that cylinders placed under apex pointing upstream position experienced less vibration and were more stable due to receiving force from the fluid in the flow field.

Several other experimental studies were conducted on oscillating triangular cylinders. However, these studies were limited to exploring several aspects of oscillating triangular cylinders only. For example, Tatsuno et al. (1990) investigated the statically stable posture of a triangular cylinder, allowing it to freely rotate around its central axis fixed perpendicular to a uniform flow while in a similar study Srigrarom and Koh (2008) observed continuous oscillation of the equilateral triangular cylinder resulting from the symmetrical flow structure using dye flow visualization and particle image velocimetry (PIV) measurements. The flow structure around the vibrobot and its impact on hydrodynamic forces were investigated through numerical simulations by Malah et al. (2016) focusing on the motion laws of the vibrobot triangular in shape with harmonic oscillation of internal mass. Zhang et al. (2016) experimentally identified three primary regions based on amplitude and frequency responses: vortex-induced vibration (VIV) branch, transition branch from VIV to galloping, and galloping branch on an elastically mounted equilateral triangular cylinder in a water channel. Similar experimental studies were conducted by Seyed-Aghazadeh et al. (2017) on flow-induced oscillations of a flexibly mounted triangular cylinder at various angles of attack. Senaei et al. (2021) investigated the stability of two-dimensional triangular cylinders with apex pointing upstream in planar flows.

Few studies have studied the boundary layer phenomenon in triangular cylinders. Fewer studies have covered 75° triangular cylinder in DOWN configuration with Re in the intermediate range. Earlier studies only indicate the presence of a stable boundary layer developed on the sides of the triangular cylinder. These studies observed the secondary vortices formed as a result of the primary corner vortices. However, this observation only suggests that these vortices play a role in the development of this boundary layer.

These studies even though limited in scope indicate that the region around the cylinder sides has fluid dynamics aspects that have not yet been investigated. The studies indicate the existence of a region where boundary layer ceases to exist in this region. The studies further indicate that the location of this region should be invariant of Re for a given geometry. This region of inactivity where the boundary layer ceases to exist has certain interesting properties. For instance, the fluid is stationary in this region making the region stable and isolated. The region is characterised by zero velocity gradient without any vorticity and

turbulence. These unique properties of this inactivity region make it an ideal location for injection of additional fluid. This location has several practical implications as follows:

- (i) Potential location for injecting additional fluid in the flow.
- (ii) Potential location for placement of probe for taking measurements.
- (iii) Active flow control.
- (iv) Drag depends on the skin friction generated because of the frictional forces between the solid surface and the boundary layer.

The identification of the region of inactivity requires a detailed investigation of the boundary layer phenomenon occurring on the sides of the triangular cylinder. Numerical techniques offer higher temporal and spatial resolution required for such an investigation. Therefore, the objective of this numerical study is to investigate 75° triangular cylinder in DOWN configuration at Re in the intermediate range. The rest of the study is outlined as follows. The first section is the introduction, which, is this section. The research problem has been introduced in this section. The literature review is provided next to provide the background information and support the research problem. The second section is the methodology section. This section gives the details about the range of parameters, governing equations, numerical study details along with the details of the software used. The third section is the results section. The numerical results are both verified by mesh refinement test and validated against published experimental results to establish the quality of the results. The next part of this section explains the results obtained. The results obtained are finally discussed in the discussions section.

2. Methodology

2.1 Range of Parameters

A triangular cylinder of apex angle 75° , as shown in Figure 1 was selected as a test case as this angle is above 60° at which no appreciable effect of Re is observed on drag coefficient (Lindsey, 1938).

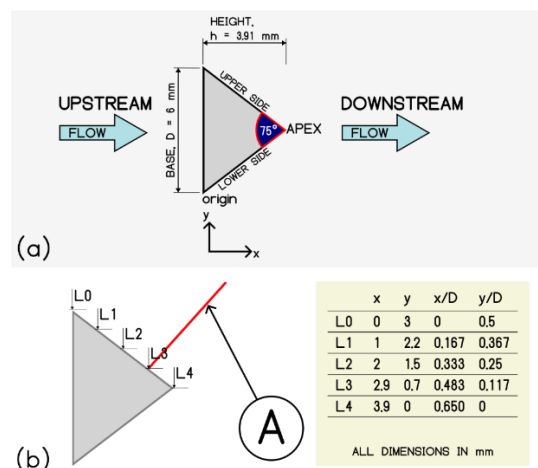


Figure 1. Details of the isosceles triangular cylinder in apex facing downstream (DOWN) configuration. (a) The dimensions of the cylinder with flow configuration. The height, $h = 3.91$ mm, base, $D = 6$ mm and apex angle = 75° . The base is the characteristic length used for Reynolds number calculations. (b) The details of the equidistant points used for extracting x -velocity profile data for the boundary layer study. The red line indicated by the letter “A” represents the line direction perpendicular to the side of the cylinder along which the velocity profile data was extracted.

Intermediate Re of 520, 620, 840 and 1040 were selected for the study. The Re are based on the base length, $D = 6 \text{ mm}$, of the triangular cylinder. The corresponding free flow velocities were 1.2, 1.5, 2.1 and 2.5 m/s . These Re correspond to Mach numbers of 0.0035296, 0.004412, 0.006177 and 0.007353 respectively. Since, flow over sharp-edged obstacles such as triangular cylinders is independent of Re over a very wide range of Re . Furthermore, at intermediate Re , the fluid is highly unstable and on the verge of becoming turbulent. This unstable flow allows the study of highly dynamic fluid structures that are not possible at laminar or fully turbulent Re . Consequently, the results obtained in this range will be more general in nature. Therefore, a set of intermediate Re was chosen. Air at 14.5°C having kinematic viscosity, $\nu = 1.50 \times 10^{-5} \text{ m}^2\text{s}^{-1}$ at this temperature, was used as fluid for both numerical study.

2.2 Governing Equations

For an unsteady, three-dimensional mass conservation equation for incompressible fluid for the mean flow resulting from time averaging the sum of mean and fluctuating component is as follows (Versteeg and Malalasekara, 2010):

$$\text{div}\mathbf{U} = 0 \quad (1)$$

where, \mathbf{U} is the mean velocity vector.

Applying the above principles on the momentum equation results in the Reynolds-Averaged Navier-Stokes equations for incompressible flow given as follows (Versteeg and Malalasekara, 2010):

$$\frac{\partial U}{\partial t} + \text{div}(U\mathbf{U}) = -\frac{1}{\rho} \frac{\partial P}{\partial x} + \nu \text{div}(\text{grad}(U)) + \frac{1}{\rho} \left[\frac{\partial(-\overline{\rho u'^2})}{\partial x} + \frac{\partial(-\overline{\rho u'v'})}{\partial y} + \frac{\partial(-\overline{\rho u'w'})}{\partial z} \right] \quad (2)$$

$$\frac{\partial V}{\partial t} + \text{div}(V\mathbf{U}) = -\frac{1}{\rho} \frac{\partial P}{\partial y} + \nu \text{div}(\text{grad}(V)) + \frac{1}{\rho} \left[\frac{\partial(-\overline{\rho u'v'})}{\partial x} + \frac{\partial(-\overline{\rho v'^2})}{\partial y} + \frac{\partial(-\overline{\rho v'w'})}{\partial z} \right] \quad (3)$$

$$\frac{\partial W}{\partial t} + \text{div}(W\mathbf{U}) = -\frac{1}{\rho} \frac{\partial P}{\partial z} + \nu \text{div}(\text{grad}(W)) + \frac{1}{\rho} \left[\frac{\partial(-\overline{\rho u'w'})}{\partial x} + \frac{\partial(-\overline{\rho v'w'})}{\partial y} + \frac{\partial(-\overline{\rho w'^2})}{\partial z} \right] \quad (4)$$

where, the six additional terms, $-\overline{\rho u'^2}$, $-\overline{\rho v'^2}$, $-\overline{\rho w'^2}$, $-\overline{\rho u'v'}$, $-\overline{\rho u'w'}$ and $-\overline{\rho v'w'}$ are Reynolds stresses; U, V, W are mean velocity components; u', v', w' are the fluctuating velocity components; P is pressure; t is time; x, y, z are Cartesian coordinates; ρ is fluid density; ν is kinematic viscosity.

The vorticity is defined as the curl of the velocity vector:

$$\boldsymbol{\omega} = \frac{1}{2} \text{curl } \mathbf{u} \quad (5)$$

and

$$\boldsymbol{\zeta} = 2\boldsymbol{\omega} \quad (6)$$

where, $\boldsymbol{\Omega}$ = angular velocity vector, s^{-1} , \mathbf{u} = velocity vector, ms^{-1} and $\boldsymbol{\zeta}$ is the vorticity.

The curl of the flow velocity shows the angular velocities and hence vorticities to be the functions of velocity gradients. There are two ways of creating a velocity gradient. First, by the no-slip condition at the solid boundary. Second, when there is a difference in velocities of two fluid layers. In the context of current study, both these conditions exist in the flow over triangular cylinder in DOWN configuration.

The first condition exists at the solid surface of the sides of the cylinder. While the second condition exists when the shear layers get forcibly separated at the sharp corners of the cylinder.

The vorticity transport equation for incompressible three-dimensional flow with constant ν is as follows:

$$\frac{D\boldsymbol{\omega}}{Dt} = (\boldsymbol{\omega} \cdot \text{grad})\mathbf{u} + \nu \nabla^2 \boldsymbol{\omega} \quad (7)$$

where, $\frac{D}{Dt}$ is the substantial derivative, $\boldsymbol{\omega}$ is angular velocity vector, \mathbf{u} is the velocity vector and ν is the kinematic viscosity. The vorticity transport equation shows us how the vorticity is transported in a flow. Substantial derivative shows us the rate of change of angular velocity field and hence vorticity with time and space. This variation in vorticity depends on the sum of the two terms on the right side of the Equation (7). The first term $(\boldsymbol{\omega} \cdot \nabla)\mathbf{u}$ represents the stretching of vorticity due to the flow velocity gradients. While the second term $\nu \nabla^2 \boldsymbol{\omega}$ is the diffusion term. The isosceles triangular cylinder has uniform cross-section. The flow over the cylinder is three-dimensional. The measurements are taken in the z -plane. Therefore, the stretching term $(\boldsymbol{\omega} \cdot \text{grad})\mathbf{u}$ vanishes in the z -plane and only z -component of angular velocity vector remains. Consequently, the vorticity transport equation simplifies to:

$$\frac{\partial \omega}{\partial t} + u \frac{\partial \omega}{\partial x} + v \frac{\partial \omega}{\partial y} = \nu \left(\frac{\partial^2 \omega}{\partial x^2} + \frac{\partial^2 \omega}{\partial y^2} \right) \quad (8)$$

where,

$$\omega = \omega_z = \frac{1}{2} \left(\frac{\partial v}{\partial x} - \frac{\partial u}{\partial y} \right).$$

In the Equation (8) there no pressure term and stretching term. Therefore, the transport of z -vorticity component depends on the kinematic viscosity in the diffusion term.

2.3 The Standard k - ε Model by Launder and Spalding (1983)

The Standard k - ε model by Launder and Spalding (1983) was used in the study. This model was selected over other turbulence models because this model is a well established model. It is computationally less expensive. The grid used for the current study is very large. Use of other turbulence models would have considerably increased the computational time. That is because use of large eddy simulation (LES) requires finer mesh for wall resolution. LES is feasible only if wall resolution is used. For wall modelling k - ε model is not only faster but also accurate. Increased mesh resolution in LES increases the already high computational time of LES.

The reliability of the numerical results was ensured by performing verification and validation studies explained in the results section. The accuracy of the model is increased by use of PISO algorithm despite increased computational cost. The geometry studied is a standard geometry with proven results obtained using k - ε model by several researchers in the past. The standard k - ε model gives satisfactory results for boundary layer flows (Shih et al., 1994). Details of PISO algorithm is explained in next section. Since the present study is focused at flow near the side walls of the triangular cylinder, the standard k - ε model was selected for the study. The following transport equations are used in this model for k and ε :

$$\frac{\partial(\rho k)}{\partial t} + \text{div}(\rho k \mathbf{U}) = \text{div} \left[\frac{\mu_t}{\sigma_k} \text{grad } k \right] + 2\mu_t S_{ij} \cdot S_{ij} - \rho \varepsilon \quad (9)$$

$$\frac{\partial(\rho \varepsilon)}{\partial t} + \text{div}(\rho \varepsilon \mathbf{U}) = \text{div} \left[\frac{\mu_t}{\sigma_\varepsilon} \text{grad } \varepsilon \right] + C_{1\varepsilon} \frac{\varepsilon}{k} 2\mu_t S_{ij} \cdot S_{ij} - \rho \varepsilon - C_{2\varepsilon} \rho \frac{\varepsilon^2}{k} \quad (10)$$

The values, $C_\mu = 0.09$, $\sigma_k = 1.00$, $C_{1\varepsilon} = 1.44$, $C_{2\varepsilon} = 1.92$, are used for the five unknown constants employed in equations.

2.4 Pressure Implicit with Splitting of Operators (PISO) Algorithm

Sharp edges of triangular cylinder result in flow separation and recirculation zones near the surface. Accurately predicting these zones and vortex shedding frequency and stability is crucial for flow analysis. The intricate flow patterns and interaction of vortices and other flow structures further complicate the situation. SIMPLE, a semi-implicit method for pressure-linked equations, faces limitations in addressing turbulent flows, accurately estimating flow separation and recirculation zones, and capturing complex flow features. To obtain reliable and accurate findings, PISO or more sophisticated algorithms are recommended. PISO's enhanced pressure-velocity coupling improves flow separation prediction, recirculation zones, and vortex shedding. Furthermore, the PISO algorithm found to be more effective in use of small time steps with Standard $k-\varepsilon$ model in comparison to SIMPLE algorithm allowing higher temporal resolution required for the study (Wanik and Schnell, 1989). Consequently, PISO algorithm was selected for study due to high-quality results despite computational cost.

2.5 Details of OpenFOAM Software Package

A computer with two cores, 6 GB RAM running Linux operating system was used for the study. OpenFOAM v5.0 was used in the study. OpenFOAM is an object-oriented framework written in C++. OpenFOAM is developed by OpenCFD Ltd. since 2004. OpenFOAM is used for numerical simulation of Continuum Mechanics. In the term OpenFOAM, "FOAM" stands for Field Operation And Manipulation. The majority of commercial CFD softwares are monolithic. That is, all functionalities are bundled into a single huge programme. As a result, there is less flexibility. In comparison to monolithic functional approaches, OpenFOAM's object-oriented approach enables modularity and flexibility. As a result, unlike other softwares having graphical user interface (GUI), OpenFOAM is command line interface (CLI) based.

Apart from being open source, OpenFOAM has some other inherent benefits. This enables extremely fine control of the mesh, boundary conditions, numerical solver and control settings. Unlike other softwares, OpenFOAM will not begin simulations unless the mesh is totally error-free. By default, OpenFOAM only works with three-dimensional meshes. Because all control parameters are defined within a text file, changing the parameters for different flow conditions is quite simple. Because of all these advantages OpenFOAM was used in the current study.

3. Results

3.1 Mesh Refinement Test

The meshing used for the numerical simulations was verified by performing mesh refinement test. Numerical simulations were performed on three of sequentially refined meshes. The number of cells were reduced by half in every direction. The total number of cells were reduced approximately by a factor of 7. The finest mesh had 1,222,800 cells, medium mesh had 158,760 and the coarse mesh had 21,980 cells, respectively. The mesh refinement test was performed on 75° triangular cylinder at $Re=1040$.

The Figure 2 compares the non-dimensionalised time-averaged x -component of velocity, u , and instantaneous turbulent kinetic energy (TKE) at time= 1.97 s at $Re = 1040$ ($U = 2.5\text{ ms}^{-1}$) for 75° triangular cylinder in DOWN configuration for the three meshes. The figures show that with every refinement the flow gets closer to the correct solution marked by the onset of the von Karman vortex street.

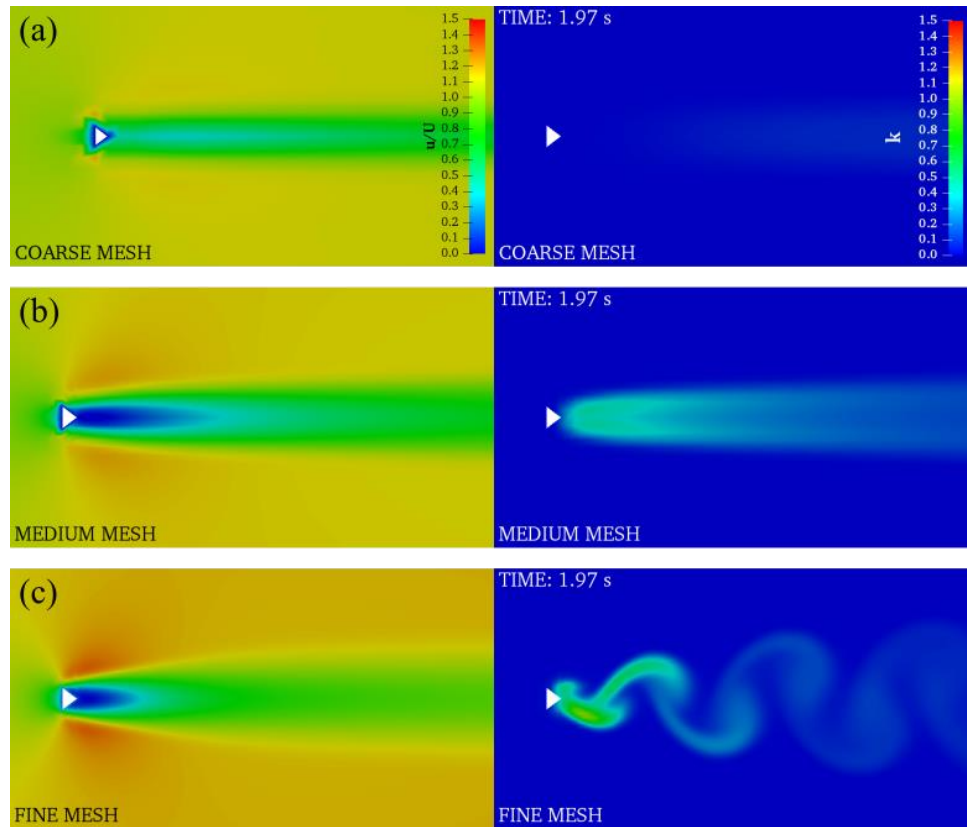


Figure 2. Comparison of non-dimensionalised time-averaged x-component of velocity, u , and instantaneous turbulent kinetic energy (TKE) at time, $t=1.97$ s at $Re = 1040$ ($U = 2.5 \text{ m s}^{-1}$) for 75° triangular cylinder in DOWN configuration for (a) coarse mesh, (b) medium mesh and (c) fine mesh. The velocity is non-dimensionalised by dividing u by free stream velocity, $U = 2.5 \text{ m s}^{-1}$.

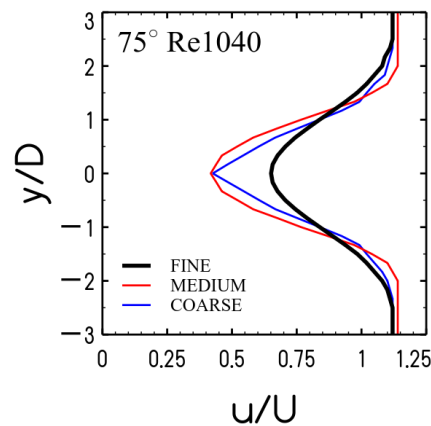


Figure 3. The figure shows a comparison between time-averaged and non-dimensionalised transverse x-component, “ u ” velocity profile at $8D$ downstream for coarse, medium and fine meshes. The velocity is non-dimensionalised by dividing u by free stream velocity, $U = 2.5 \text{ m s}^{-1}$. The y -axis distance, y , is non-dimensionalised by dividing it by base, $D = 6 \text{ mm}$.

Transverse x -component of velocity profiles were extracted from the time-averaged x -component of velocity plots of Figure 2. These profiles for coarse, medium and fine meshes are plotted in Figure 3. These profiles were extracted at $8D$ distance downstream. The bell-shaped curved can be observed for the fine mesh. This curve establishes the results obtained from the finest mesh.

The comparison of the test results established that the mesh that is being used has been sufficiently refined to resolve the flow structures for the problem undertaken. The finest mesh is validated in the next section.

3.2 Comparison of Numerical Data with Experimental Data

The finest mesh verified in the previous section through mesh refinement test is validated in this section. The Figure 4 shows the overall mesh, mesh in three dimensions and the close-up of the mesh used in present study, respectively. Mesh generated for numerical experiments was 400 mm long, 160 mm wide and 100 mm in height corresponding to PIV experiments. A three-dimensional mesh of 300 by 100 by 40 cells ($12,22,800$ cells; finest mesh established in previous section) was used for the numerical simulations. The simulations were run for a sufficiently long time for achieving steady state.

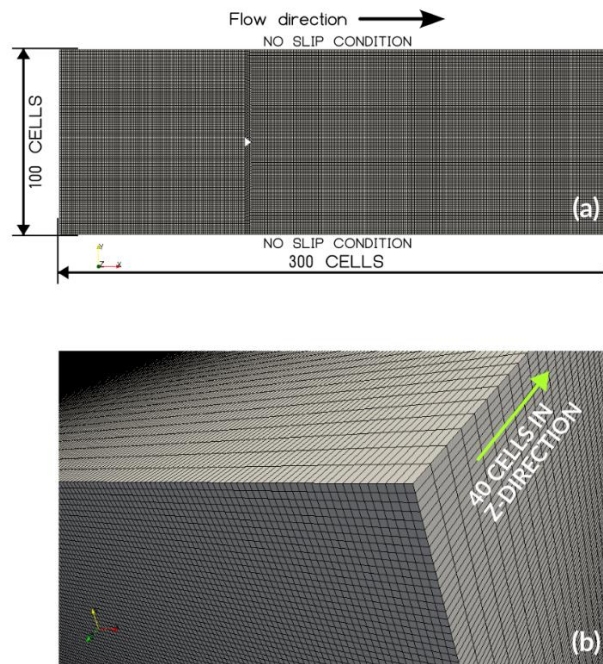


Figure 4. Details of three-dimensional mesh used in numerical simulations. (a) The figure shows the two-dimensional view of the mesh, number of cells in both x and in y -direction and the faces where the no-slip condition is applied. The direction of flow is from left to right. (b) The figure shows the three-dimensional view of the mesh with the number of cells in z -direction.

Since, no appreciable effect of Reynolds number on a triangular cylinder of apex angle 75° over 60° has been observed on drag coefficient (Lindsey, 1938). Moreover, PIV results obtained experimentally by Agrawal et al. (2013, 2016) were available for 60° . As a result, the numerical results were compared with this study. These experimental results were also used by Yagmur et al. (2017) as reference in their study.

Separate numerical simulations on the mesh having same number of cells were performed exclusively for experimental verification. The “checkMesh” utility was used for checking the finest mesh quality prior to running simulations. Some checkMesh parameters are tabulated in the Table 1. Due to the large computational time required for performing simulations on the selected mesh (total number of cells = 12,22,800) the simulation was first run on a 2D mesh consisting of 300 by 100 cell mesh and compared with experimental data. Once the mesh looked promising, the mesh was finally converted into a 3D mesh of 300 by 100 by 40 cells.

Table 1. Selected values of geometry check performed using Open FOAM check Mesh utility.

Mesh Geometry	Values
Total number of cells	1222800
Boundary openness	(1.64243e-15 7.92863e-14 -6.75202e-15)
Max cell openness	2.15402e-16
Max aspect ratio	1.5281
Minimum face area	9.7402e-07
Maximum face area	4.79989e-06
Min cell volume	3.89608e-09
Max cell volume	4.21053e-09
Total cell volume	0.00479751
Max mesh non-orthogonality	29.752
Average mesh non-orthogonality	1.82251
Max skewness	0.412178

3.2.1 Experimental Set-up Details

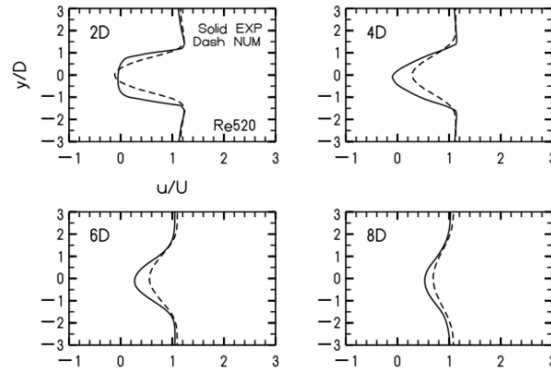
The Acrylic test section of the wind tunnel used for PIV measurements was 1500 mm long, 160 mm wide and 100 mm in height. The triangular cylinder had an apex angle of 60° with 6 mm base. The aspect ratio was 26.7 (160/6) with a blockage ratio of 6%. Reynolds numbers based on base length were 520, 640, 840 and 1040 in the intermediate range. A double pulsed Nd-YAG laser (New Wave lasers; wavelength = 532 nm; 50 mJ) was used for LASER light sheet. Olive oil seeding particles were produced by a six-jet atomizer (TSI model 9306). Powerview Plus 4MP CCD camera (2048 × 2048 effective pixels) was used for capturing PIV images. Minimum frame straddling time for PIV capture was 200 ns. A pitot-static tube and digital micro-manometer were used for validation of the velocity measured by PIV. The velocity signal from HWA, by Dantec Streamline pro, was used for measuring the Strouhal number and the power spectra. The single wire straight probe was used for the velocity signal measurements. The sampling frequency was 1000 Hz and the signal length was 20 s.

The time-averaged transverse x -component of velocity profiles were used in the study. This is because velocity profile provides information about entrainment and boundary layer. These plots are used in conjunction with TKE plots and vorticity in the current study. As a result, a comparison with experimental transverse velocity plots can reliably establish the accuracy of numerical results.

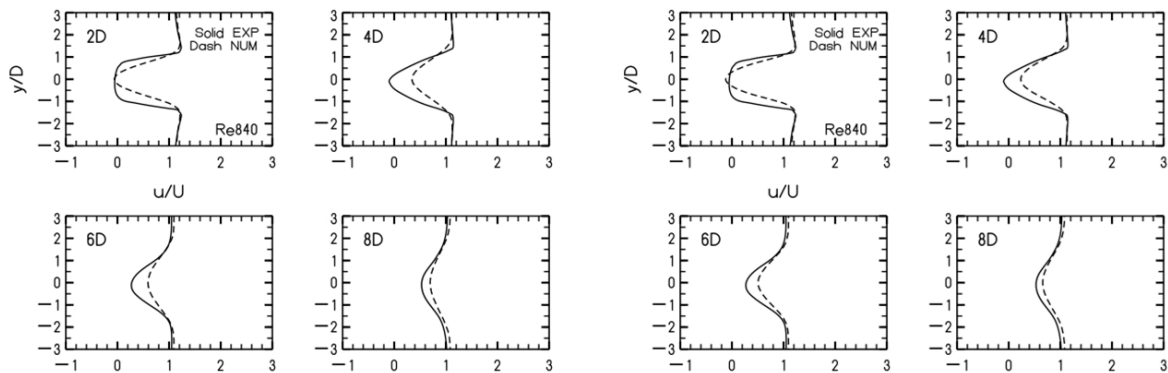
A comparison between numerical and experimental data of x -component of velocity for a triangular cylinder with apex angle of 60° in DOWN configuration at $Re = 520$ is shown in Figure 5(a). There is a good agreement between numerical and experimental results.

The standard $k-\varepsilon$ model gives satisfactory results for boundary layer flows but is not suited for flows with a high mean shear rate or a massive separation (Shih et al., 1994). Therefore, the slight discrepancy observed in the plots may be due to the presence of high mean shear rate in these regions.

Results of the present study can now be discussed having established through both verification and validation studies of the current numerical model.



(a) Time-averaged non-dimensionalised transverse x-component of velocity, u , profiles at $Re=520$ at $x=2D$, $4D$, $6D$ and $8D$ downstream locations in DOWN configuration using 3d mesh.



(a) Time-averaged non-dimensionalised transverse x-component of velocity, u , profiles at $Re=840$ at $x=2D$, $4D$, $6D$ and $8D$ downstream locations in DOWN configuration using 2d mesh.

(a) Time-averaged non-dimensionalised transverse x-component of velocity, u , profiles at $Re=840$ at $x=2D$, $4D$, $6D$ and $8D$ downstream locations in DOWN configuration using 3d mesh.

Figure 5. Comparison of numerical data with experimental data. Where $2D$ is the distance two times the base length, $D = 6mm$. The distances $4D$, $6D$ and $8D$ are defined, similarly. The x -component of velocity, u , is non-dimensionalised by dividing u by free-stream velocity, U . While the distance in y -direction, y , has been non-dimensionalised by dividing y by D .

3.3 Instantaneous Turbulent Intensities and Vorticities

The nomenclature of vortices used in the study is explained in Figure 6. The vortices are labelled as upper and lower according to the upper and lower sides of the cylinder where they are formed. The primary vortices are those that are formed first. The primary vortices result in formation of secondary vortices having opposite sense of rotation. As can be seen from the legend, the blue colour denotes negative vorticity having clockwise sense of rotation while the red colour denotes the positive vorticity having counter-clockwise sense of rotation. The white arrows in the figure show the sense of rotation of the vortices.

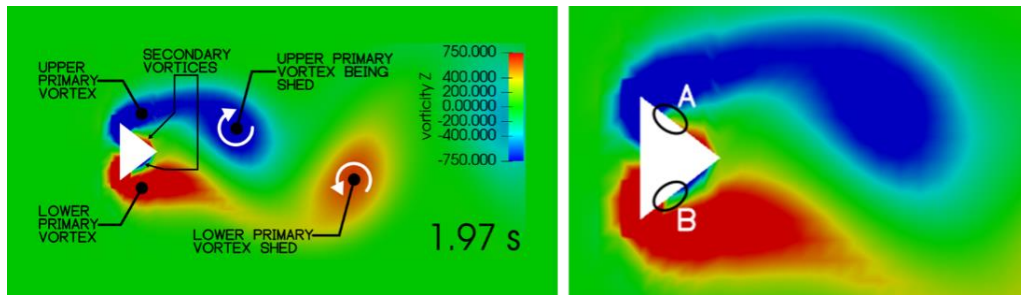


Figure 6. Nomenclature of primary and secondary vortices used in the study. The white arrows show the sense of rotation of the vortices. The region of inactivity identified by black ellipses in representative vorticity plot. The region marked by the letter A is located on the upper side of the triangular cylinder while the region marked by the letter B is located on the lower side of the triangular cylinder.

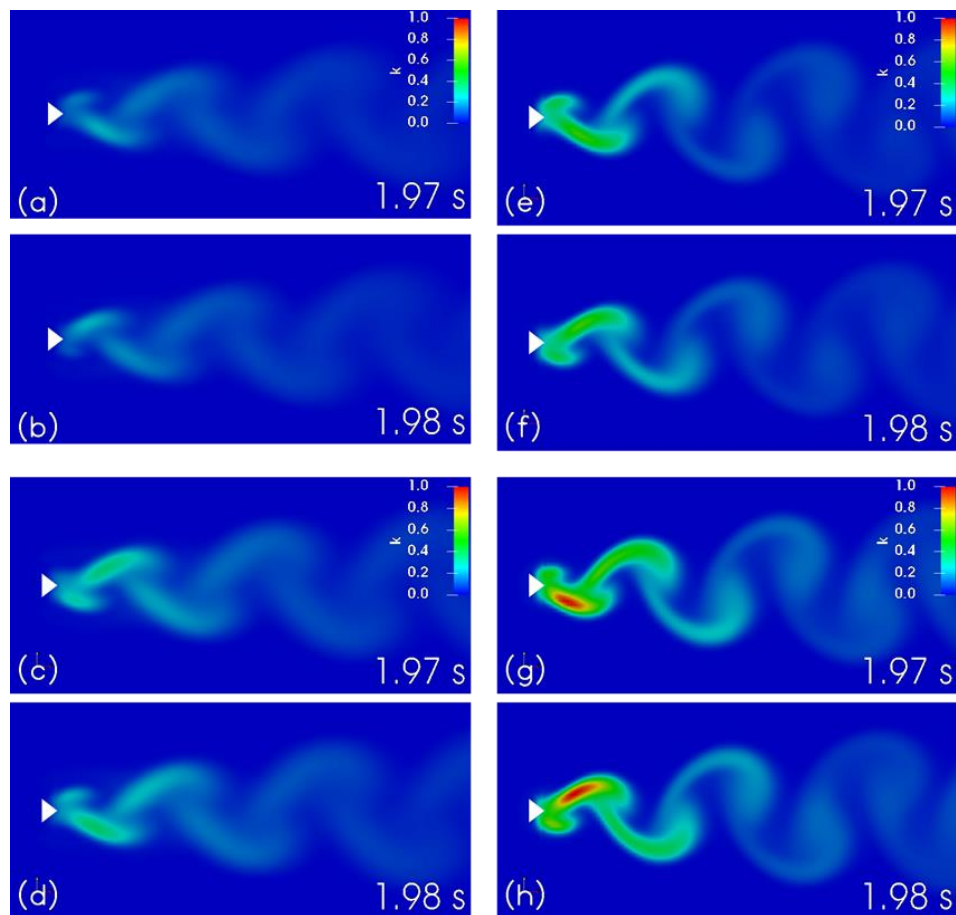


Figure 7. Instantaneous turbulent intensities at (a, b) $Re = 520$ (c, d) $Re = 640$ (e, f) $Re = 840$ (g, h) $Re = 1040$.

Figure 7 shows instantaneous turbulent intensity plots. The Figure 7(a) shows lowest turbulent intensity on and near the both cylinder walls while increased turbulence is observed away and downstream from the wall. This state remains consistent with increase in time step. If the remaining Figures 7(c), (e) and (g)

are carefully observed on and near the cylinder walls, it can be seen that the turbulence intensity tends to increase from the apex of the cylinder moving backwards to the sharp edges. This phenomenon is most prominent in Figure 7(g) with the highest Re . Even though TKE tends to increase with increase in Re , for the same Re the TKE on the cylinder wall starting from the apex is low than the rest of the fluid dynamic region. However, there is a region where the TKE always remains equal to zero irrespective of the Re . This region, shown in the Figure 6, can be seen in all the TKE and vorticity plots irrespective of Re . This region suggests absence of any boundary layer.

Figure 8 show streamlines superimposed on instantaneous x-velocities denoted by u . These velocities were non-dimensionalised by dividing with free stream velocity, $U = 2.5 \text{ ms}^{-1}$. These streamline plots support the observed area of inactivity present on either side of the cylinder. The streamlines are not present in these inactivity areas. The recirculation zones indicating vortices can be seen in these plots. These recirculation zones form the boundary of the inactivity regions.

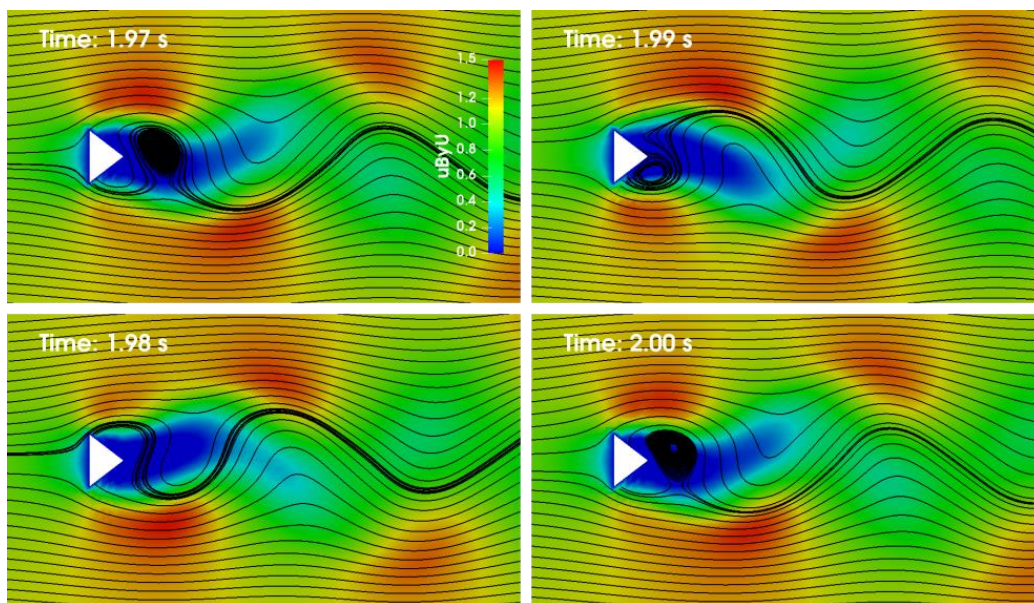


Figure 8. Streamlines superimposed on non-dimensionalised instantaneous x-velocities at $Re = 1040$. These velocities were non-dimensionalised by dividing with free stream velocity, $U = 2.5 \text{ ms}^{-1}$.

Figure 9 shows instantaneous z-component of vorticity for $Re = 520, 640, 840$ and 1040 . Figure 9(a) shows the presence of two primary vortices and two secondary vortices. Considering one side of the cylinder the secondary vortex has opposite sign to that of the primary vortex. Shedding of upper primary vortex can be observed. The figure also shows that the secondary vortices are formed simultaneously and almost in the middle of the side close to the rear corner. Figure 9(b) shows that after the upper primary vortex has been shed the lower secondary vortex has grown in size and is now feeding the upper primary vortex while the shedding of the lower primary vortex is in progress. The primary vortex that is about to shed provides energy to the secondary vortex which is then fed to the opposite primary vortex. While this secondary vortex feeds the primary vortex of same sign this phenomenon causes a reduction in the size of the secondary vortex of opposite sign. The process is finally repeated. This observation supports the behaviour of TKE observed earlier. These figures confirm the existence of a small region of inactivity indicated by the TKE plots.

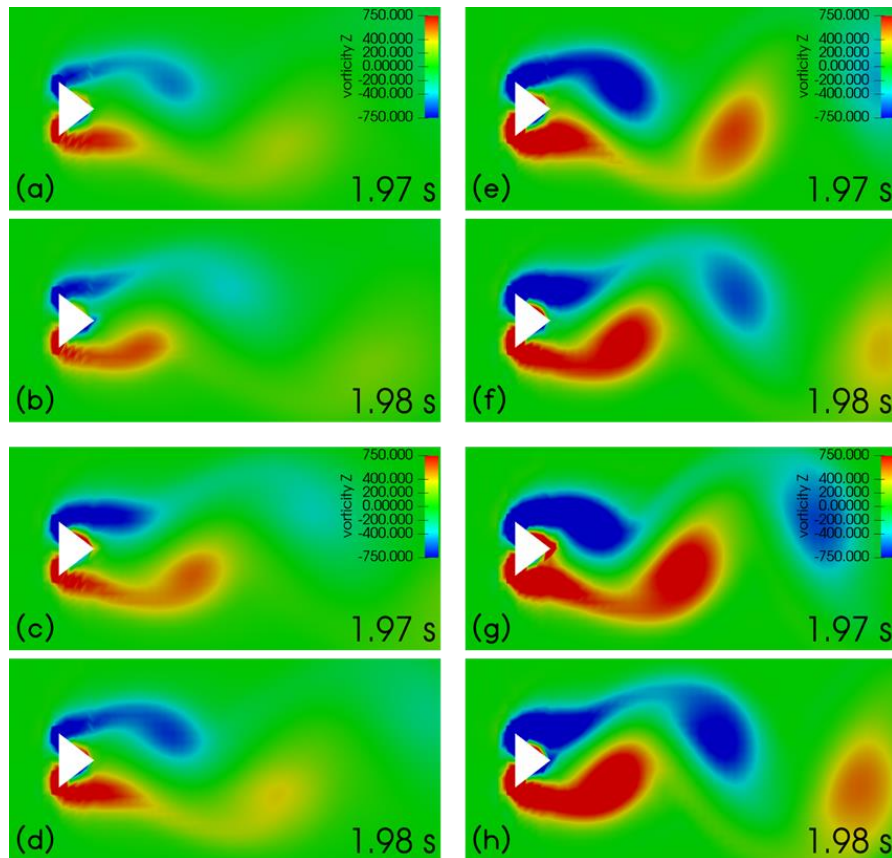


Figure 9. Instantaneous z-component of vorticity at (a, b) $Re = 520$ (c, d) $Re = 640$ (e, f) $Re = 840$ (g, h) $Re = 1040$.

A similar phenomenon is observed in Figure 7(c) at $Re = 640$. Here also the primary vortex induces and feeds energy to the secondary vortex of opposite sign. This energy is then fed to the other primary vortex by the secondary vortex thereby suppressing the secondary vortex of opposite sign. Location of the secondary vortex, as well as simultaneous formation, are similar to $Re = 520$. The only difference that can be found is an increase in vorticity due to the increase in Re .

In Figure 9(e), the flow structure at $Re = 840$ is slightly different from $Re = 520$ and 640 . Formation of primary vortices accompanied by the simultaneous formation of secondary vortices is similar to above cases. However, now the secondary vortices no longer feed the primary vortices. In Figure 9(g), the flow structure is similar but certain distinct changes can be observed at $Re = 1040$. Here the secondary vortex is feeding the primary vortex but after the primary vortex is shed like $Re = 520$ and 640 . Increase in strength of vortices is observed with increase in Reynolds number. The behaviour and size of secondary vortex supports the hypothesis of non-existence of boundary layer in the region of inactivity identified above with zero TKE.

3.4 Steady-State Instantaneous X-Velocity Component Profile at Equidistant Locations on Downstream Cylinder Surface

Figure 10 shows instantaneous u/U profiles, where u is the x -component of velocity and U is the free stream velocity, at five equidistant positions (equidistant positions are shown in Figure 1) at time, $t=2.00$ s

for all Reynolds numbers. These profiles show boundary layer development at the upper surface of the triangular cylinder. The region of inactivity observed above lies roughly between $L1$ and $L2$ depending on the Re . The Figures 9 sheds more light on the phenomenon. It can be seen that the velocity profiles on and close to the cylinder walls are invariant of the Re and also the dynamics of the region do not affect these velocity profiles. This is evident from these figures as these velocity profiles are extracted from instantaneous plots. The transient behaviour starts at some distance away from the wall. Very close to the wall and on the wall a stable region with zero to very low TKE exists.

It is observed that the primary vortices result in the development of the boundary layer close to the surface of the cylinder starting from $L4$ (apex) in the direction opposite to the flow direction up to point $L1$ where it get separated. The separation point for this boundary layer is observed at approximately $L1$, where the x -component of velocity is becomes equal to zero, irrespective of the Reynolds number. The $L1$ also marks the start boundary of the region of inactivity identified above. Since this separation is independent of Reynolds number and the rest of the flow structure, it is assumed that the boundary layer development depends on the geometry and hence the apex angle.

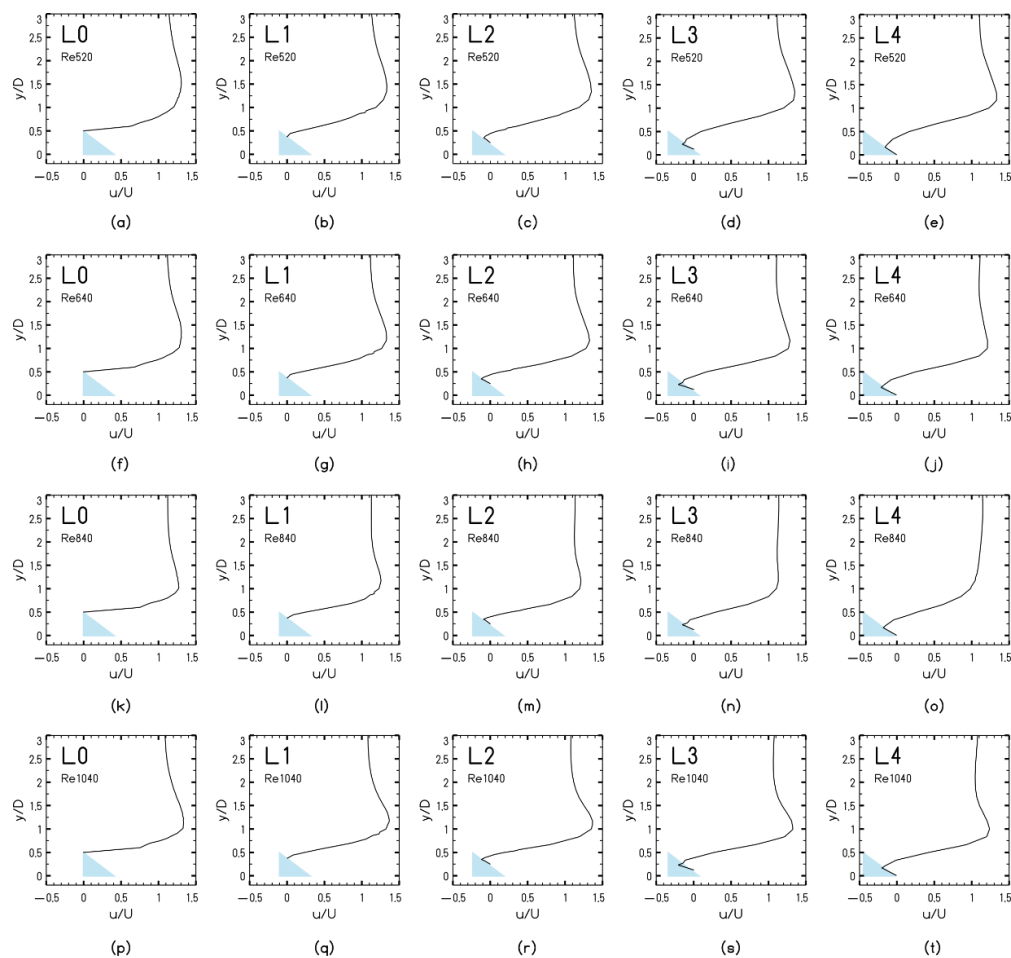


Figure 10. Instantaneous x-velocity component profile at equidistant locations on downstream cylinder surface at steady state at $Re = 520, 640, 840$ and 1040 . The half blue triangle indicates the starting point of the line on the upper side of the triangular cylinder along which the data for velocity profile was extracted. The line was normal to the side of the triangular cylinder instead of being parallel to the base.

3.5 Steady-State Instantaneous Z-Component of Vorticity at Equidistant Locations on Downstream Cylinder Surface

Boundary layer development can be observed at the downstream surface of the cylinder. Since, the velocity profiles are qualitatively same for all Reynolds numbers. Boundary layer patterns are similar at all Reynolds numbers. Increase in Reynolds number cause increase in TKE and hence delayed boundary layer separation. At $Re = 840$ the velocity profile at $L4$ is different than at $Re = 520, 640$ and 1040 .

From Table 2 it can be observed that separation occurs at $x \approx L2$ that is close to the middle point of one side of the cylinder. This is the place of formation of the secondary vortex. This position is irrespective of change in Reynolds number. However, the vortex strength increases with increase in Re .

Table 2. Points of inflection of ω_z .

	Points of Inflection (y/D) of ω_z .			
	$Re = 520$	$Re = 640$	$Re = 840$	$Re = 1040$
L0	1.628	1.424	1.017	1.119
L1	1.634	1.227	1.179	1.179
L2	0.444 (S) and 1.584	0.444 (S) and 1.18	0.404 (S) and 1.172	0.427 (S) and 1.164
L3	0.421 (S) and 1.514	0.404 (S) and 1.177	0.363 (S) and 1.349	0.388 (S) and 1.004
L4	0.384 (S) and 1.334	0.0375 (S) and 0.112	0.358 (S) and 3.775	0.342 (S) and 1.05

Table 3 shows the ratio between maximum vortex strength of primary and secondary vortices. It is observed that the ratio lies in the range 1.1-1.5 and the average value is 1.2. The Table 3 supports the qualitative observation that the flow structure is independent of Re . From Tables 2 and 3 a relationship independent of Re is proposed:

$$\text{Point of separation} \approx \frac{h}{2} \quad (11)$$

$$\text{Location of secondary vortex} \approx \frac{h}{2} \quad (12)$$

$$|\omega_z^1| = 1.2 \times |\omega_z^2| \quad (13)$$

Table 3. Ratio of z-component of primary and secondary vortices at $L2$.

Re	Primary Vortex	Secondary Vortex	Ratio
520	457	574	1.3
640	774	832	1.1
840	797	1205	1.5
1040	1224	1390	1.2
Average ratio			1.2

Figure 11 shows instantaneous z-component of vorticity at equidistant locations on downstream cylinder surface. Similar vorticity profiles can be observed for different Reynolds numbers. Increase in Reynolds number results in increased vorticity strength. This shows that a common flow is present with few parameters affected by an increase in Reynolds number. Even though the flow gets separated at sharp edges boundary layer is developed at the surface of the cylinder downstream. The vorticity strength tends to increase with an increase in Re but reduces at $L4$ at $Re = 840$. Then again increases at $Re = 1040$ at $L4$.

At $L0$ increase in vortex strength with increase in Reynolds number is observed. This is the point of separation of free shear layers. The free shear layers engulf the side wall of cylinder up to $L1$ at all Re . The onset of the secondary vortex is observed at $L2$ that continues up to $L4$, the apex of the triangular

cylinder at all Reynolds numbers. From Figure 9, the vorticity contours show that this secondary vortex of a sign opposite to that of the primary vortex is formed simultaneously on both sides. However, the strength of secondary vortex depends on Reynolds number. The strength of secondary vortex increases with increase in Reynolds number. The secondary vortex tends to engulf the apex of the triangular cylinder and feed the primary vortex of the same sign on the opposite side. As the strength increases the secondary vortex starts feeding the opposite primary vortex of same sign and after this primary vortex is shed. It can also be observed from the vorticity contours that minimum size secondary vortex form simultaneously on both sides and their strength increases alternatively coupled with alternate vortex shedding.

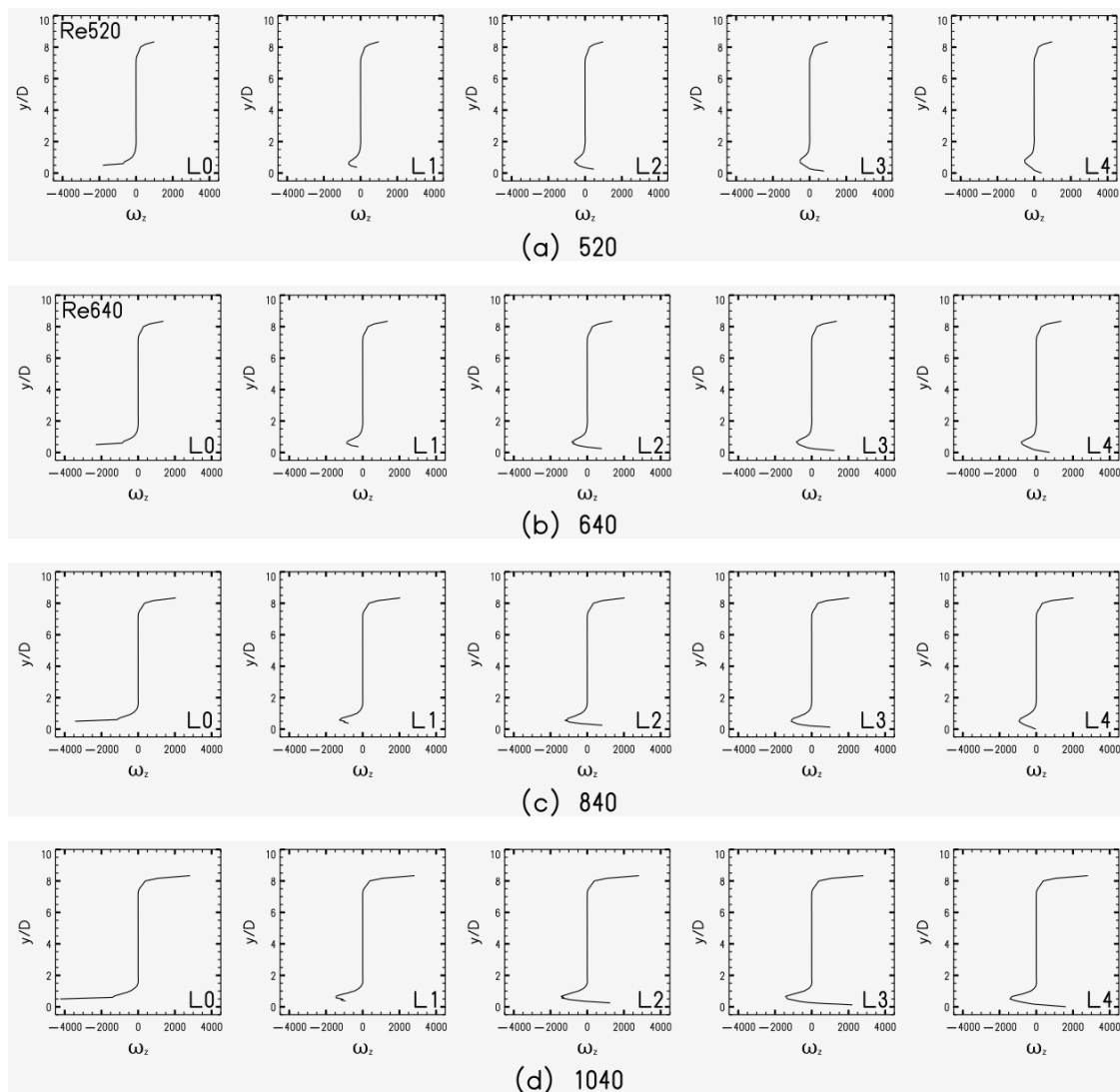


Figure 11. The z-component of vorticity at (a) $Re = 520$, (b) $Re = 640$, (c) $Re = 840$ and (d) $Re = 1040$.

At $Re = 840$ though the formation of the secondary vortex on either side was observed, the secondary vortices were not found to feed the primary vortices, unlike other three Re .

4. Discussions

Entrainment is a complex fluid dynamic phenomenon resulting from boundary layer. It describes how surrounding fluid mixes into a flow upon interaction. Factors such as velocity gradient and turbulence affect entrainment. The boundary layer plays a crucial role in the entrainment process. The rate of entrainment is related to the rate of change of the velocity or velocity gradient in the boundary layer. The rate of change of the velocity gradient indicates how quickly the velocity changes in a given direction. Regions with high velocity gradients are potential sites for increased entrainment. A significant change in velocity along a direction perpendicular to the flow indicates lateral motion of fluid into or out of the wake. This lateral fluid motion contributes to entrainment.

4.1 Entrainment and Instantaneous Transverse x -Component of Velocity Profiles

The transverse (sideways) x -component of the velocity is measured perpendicular to the main flow direction of the fluid over a period of time. The gradient or derivative of the transverse velocity with respect to the lateral direction gives the rate of change of the transverse velocity. The variation of this rate of change in space gives an insight into the dynamics of fluid entrainment and wake development. Graphical representations of the transverse velocity profiles at various downstream locations are shown in Figure 10. These profiles show the variation in transverse velocity along the top of the cylinder. The peak transverse velocities at certain locations highlight the regions of maximum entrainment. The peak starts at location $L2$ and increases to a maximum at $L4$. This peak indicates the start of entrainment at $L2$ and maximum entrainment at $L4$. This increasing transverse velocity profile suggests increasing fluid entrainment as the flow progresses downstream.

4.2 Entrainment and TKE

TKE plots are shown in Figure 7. TKE is a measure of the energy associated with turbulent fluctuations in the flow. TKE plots provide insights into the intensity of turbulence within the wake. Correlating TKE data with transverse velocity profiles reveal how turbulence levels influence entrainment patterns. Higher TKE regions show increased entrainment. The Figure 7 shows an increase in TKE with increase in Reynolds number implying increased rate of entrainment with increase in Reynolds number.

4.3 Entrainment and Vortex Formation

Entrainment is associated with the formation of vortices. The entrainment process is particularly evident when vortices shed from the cylinder interact with the surrounding fluid. This interaction results in transverse motion of the fluid into the wake. The peak transverse velocities discussed above indicate regions of intense entrainment and are associated with the strongest vortices shown in the Figure 9. The figure shows that even though the vortices become stronger with increase in Re , the region of inactivity remains unaffected.

4.4 Boundary Layer, Entrainment and Region of Inactivity

TKE plots, when used in conjunction with transverse velocity profiles and vorticity, offer a comprehensive understanding of the fluid dynamics in the wake behind a cylinder. In the vicinity of an object, the boundary layer experiences changes in velocity and pressure gradients. This leads to the development of shear layers and vortices. These shear layers and vortices are inherent to boundary layer dynamics. They contribute to the entrainment of fluid into the wake.

The Figure 10 identifies the region of inactivity to be located between the points $L1$ and $L2$. This region is identified by the absence of the peak of transverse velocity profile between these two locations. This region is further identified by the absence of vorticity in Figure 9 and zero TKE at $L2$. The region beyond

$L2$ marks the end of boundary layer. The Figure 10 shows that the boundary layer starts in reverse from $L4$ and ends at $L2$ passing through $L3$.

The Figure 7 shows an increase in TKE with increase in Reynolds number implying increased rate of entrainment with increase in Reynolds number. The Figure 11 shows that even though the vortices become stronger with increase in Re , the region of inactivity remains unaffected. This implies that the region of inactivity and its location $L2$ is invariant of Re .

4.5 Practical Implications

The unique properties of the region of inactivity makes it an ideal location for injection of additional fluid and has following practical implications as discussed below:

- (i) Potential location for injecting additional fluid in the flow. There are two example applications where additional fluid needs to be injected in the fluid stream. Sometimes fluid needs to be injected without disturbing the original flow. Like fuel needs to be injected with minimal disturbance to the original flow. The fluid in region of inactivity is not only isolated but also stationary. Consequently, this forms a potential point for injecting additional fluid in the original flow with minimal disturbance to the original flow.
- (ii) Potential location for placement of probe for taking measurements. Measurement of several flow parameters like velocity and pressure require insertion of some kind of physical probe in the flow. This disturbs the flow and its properties. These probes cannot take measurements without disturbing the flow. The minimal disturbance by the probe is required for taking accurate and precise measurements. The fluid in region of inactivity is isolated from the surrounding flow. As a result, it is a potential location for placement of measurement probes causing minimal disturbance to the original flow.
- (iii) Active flow control. The fluid needs to be injected to intentionally disturb the flow. Like actively controlling the original flow requires to disturb the flow by injecting additional fluid in the flow. The region of inactivity provides a potential location for injecting additional fluid. Drag reduction by introduction of additional fluid. This application is related to active flow control.
- (iv) Drag depends on the skin friction generated because of the frictional forces between the solid surface and the boundary layer. Boundary layer can be controlled by injecting additional fluid at the region of inactivity. Boundary layer control has the potential to reduce drag. The current study shows one potential location where additional fluid can be injected to control the flow structure and hence reduce drag.

The ratio between maximum vortex strength of primary and secondary vortices has physical implications and is practically important. This ratio is a characteristic inherent to the isosceles triangular cylinder with apex pointing downstream. In practical applications with variable flow velocities this independence of primary to secondary vorticity ratio from Reynolds number allows bluff body to be designed only once. This is because the same bluff body will work over a wide range of flow velocities and hence Reynolds numbers. Design of any application involving this geometry will benefit from the result.

The discovery made in the current study was indicated by the early researchers. For instance, the effect of various factors studied by El-Sherbiny (1983), Nakagawa (1989), El Wahed et al. (1993) and Iungo and Buresti (1989) on boundary layer behaviour pointed towards existence of phenomenon. This unexplored phenomenon is crucial for the understanding of the fluid dynamics and performance optimisation of triangular cylinders. The studies undertaken by Djebedjian (2002), Camarri et al. (2006), Rui et al.

(2019), Derakshandeh and Alam (2019) and Feshalalmi et al. (2022) on wake features, vorticity and flow variations in bluff bodies also indicated an existence of such a phenomenon.

The multiple studies undertaken by Iungo and Buresti (2003), Buresti and Iungo (2008) and Buresti and Iungo (2010) and further carried by Iungo and Lombardi (2011) highlighted the complexity of the above phenomenon. Mahato et al. (2018) and Seyed-Aghazadeh et al. (2017) implied the connection between the boundary layer and vortex shedding behaviour and the role of boundary layer in shaping wake dynamics, vortex shedding patterns and flow behaviour around triangular cylinder. Cheng and Liu (2000) and Wang et al. (2019b) found that the flow interacts with the boundary layer as it circulates on the sides of the cylinder.

5. Conclusion

The 75° triangular cylinder in DOWN configuration at intermediate $Re = 520, 640, 840$ and 1040 was investigated numerically. The boundary layer phenomenon on the sides of the cylinder was studied. The main objective was to identify the region of inactivity. Detailed boundary layer analysis and entrainment was done for identification of the region. The practical implications of the findings were finally discussed. A region of inactivity was found to exist on either side of the cylinder. The boundary layer is non-existent in this region. This region was identified as the region with zero TKE and vorticity. The inactivity region as determined from the instantaneous transverse x -component of velocity profiles was found to lie between $L1$ and $L2$. This location is invariant of the Reynolds number. Moreover, the region remains unaffected by transient fluid dynamic behaviour occurring downstream.

This finding has many practical implications. The inactivity region can serve as a potential location for injecting additional fluid in the flow and for placement of a measurement probe. The location can be used for active control of flow and reducing drag.

The additional fluid to be injected can be channelled from inside the bluff body itself. This possibility offers a great convenience and advantage in design of applications involving active flow control and drag reduction techniques that involve injection of additional fluid to disrupt the flow for controlling. The fluid can not only be injected but also sucked for flow control. The isolated region of inactivity also opens up possibility of fluid suction for the development of active flow control and drag reduction technologies. The isolation of the inactivity region offers another convenience of probe insertion with minimal disruption of the flow. This region opens up another set of possible applications.

The relationship between primary and secondary vortices was an additional finding. The ratio of modulus of absolute primary z -component of vorticity, $|\omega_z^1|$, to the modulus of secondary z -component of vorticity, $|\omega_z^2|$, was found to be approximately equal to 1.2. The ratio was found to be nearly consistent across the Reynolds number range considered in the study.

This independence allows a bluff body to be designed only once. The same bluff body can work over a wide range of flow velocities and Reynolds numbers. Design of any application involving this geometry will benefit from the result.

Future scope of work can be focussed on further research and experimentation to explore these practical applications in different engineering and fluid dynamics contexts. The current study has provided a potential location for insertion of a measurement probe that should result in minimum interference in the flow while the measurements are being taken. However, this inference needs further experiments to be established. Similarly, the discovery of the ratio has been established for the current range of parameters.

Even though the Reynolds number independence is well-established and implies that the bluff body designed once would work for a wide range of Reynolds numbers, this requires further experiments to actually show that the phenomenon is actually occurring. The field of technologies involving active flow control and drag reduction is very wide. Our discovery of the region of inactivity has opened up several new possibilities that can and needs to be explored further for the development of new active flow control and drag reduction technologies.

Conflict of Interest

The authors confirm that there is no conflict of interest to declare for this publication.

Acknowledgments

The authors would like to acknowledge Graphic Era University for providing all the research facilities and its continuous support for the present research work.

References

- Agrawal, N., Dutta, S., & Gandhi, B.K. (2013). An experimental study on flow past an equilateral triangular prism at intermediate Reynolds number and the effect of its orientation. In *Fluids Engineering Division Summer Meeting* (Vol. 55553, p. V01BT13A005). American Society of Mechanical Engineers. <https://doi.org/10.1115/FEDSM2013-16474>.
- Agrawal, N., Dutta, S., & Gandhi, B.K. (2016). Experimental investigation of flow field behind triangular prisms at intermediate Reynolds number with different apex angles. *Experimental Thermal and Fluid Science*, 72, 97-111.
- Buresti, G., & Iungo, G.V. (2008). Flow fluctuations and vorticity dynamics in the near-wake of a triangular prism in cross-flow. In *Proceedings of International Colloquium on Bluff Body Aerodynamics and Applications* (pp. 20-24). Milano, Italy.
- Buresti, G., & Iungo, G.V. (2010). Experimental investigation on the connection between flow fluctuations and vorticity dynamics in the near wake of a triangular prism placed vertically on a plane. *Journal of Wind Engineering and Industrial Aerodynamics*, 98(6-7), 253-262.
- Buresti, G., & Lombardi, G. (2003). Experimental analysis of the upper-wake flow field of finite cylinders with triangular and circular cross-section. In *Atti XVI Congresso AIMETA* (Vol. 1, pp. 1-10).
- Camarri, S., Salvetti, M.V., & Buresti, G. (2006). Large-eddy simulation of the flow around a triangular prism with moderate aspect ratio. *Journal of Wind Engineering and Industrial Aerodynamics*, 94(5), 309-322.
- Cheng, M., & Liu, G.R. (2000). Effects of afterbody shape on flow around prismatic cylinders. *Journal of Wind Engineering and Industrial Aerodynamics*, 84(2), 181-196.
- Derakhshandeh, J.F., & Alam, M.M. (2019). A review of bluff body wakes. *Ocean Engineering*, 182, 475-488.
- Djebedjian, B. (2002). Numerical investigation on vortex shedding flow behind a wedge. In *Fluids Engineering Division Summer Meeting* (Vol. 36150, pp. 617-627). Quebec, Canada.
- El Wahed, A.K., Johnson, M.W., & Sproston, J.L. (1993). Numerical study of vortex shedding from different shaped bluff bodies. *Flow Measurement and Instrumentation*, 4(4), 233-240.
- El-Sherbiny, S. (1983). Flow separation and reattachment over the sides of a 90 triangular prism. *Journal of Wind Engineering and Industrial Aerodynamics*, 11(1-3), 393-403.
- Feshalami, B.F., He, S., Scarano, F., Gan, L., & Morton, C. (2022). A review of experiments on stationary bluff body wakes. *Physics of Fluids*, 34(1), 011301. <https://doi.org/10.1063/5.0077323>.

- Iungo, G.V., & Buresti, G. (2009). Experimental investigation on the aerodynamic loads and wake flow features of low aspect-ratio triangular prisms at different wind directions. *Journal of Fluids and Structures*, 25(7), 1119-1135.
- Iungo, G.V., & Lombardi, E. (2011). Time–frequency analysis of the dynamics of different vorticity structures generated from a finite-length triangular prism. *Journal of Wind Engineering and Industrial Aerodynamics*, 99(6-7), 711-717.
- Jusoh, M.Z.M., AR, N.A., & Md Nor, M.W. (2020). Computational analysis of fluid flow past a bluff body at low Reynolds number in different Apex Angle. *ESTEEM Academic Journal*, 16, 65-74.
- Lauder, B.E., & Spalding, D.B. (1983). The numerical computation of turbulent flows. In *Numerical Prediction of Flow, Heat Transfer, Turbulence and Combustion* (pp. 96-116). <https://doi.org/10.1016/B978-0-08-030937-8.50016-7>.
- Lindsey, W.F. (1938). Drag of cylinders of simple shapes. *National Advisory Committee for Aeronautics Technical Report*, 619, 169-176.
- Luo, S.C., Yazdani, M.G., Chew, Y.T., & Lee, T.S. (1994). Effects of incidence and afterbody shape on flow past bluff cylinders. *Journal of Wind Engineering and Industrial Aerodynamics*, 53(3), 375-399.
- Mahato, B., Ganta, N., & Bhumkar, Y.G. (2018). Direct simulation of sound generation by a two-dimensional flow past a wedge. *Physics of Fluids*, 30(9).
- Malah, H., Chumakov, Y.S., & Movafagh, S.R. (2016). Oscillating motion of triangular cylinder in a viscous fluid. *International Journal of Coastal, offshore and Environmental Engineering*, 1(4), 19-25.
- Nakagawa, T. (1989). Vortex shedding mechanism from a triangular prism in a subsonic flow. *Fluid Dynamics Research*, 5(2), 69-81.
- Ng, Z.Y., Vo, T., Hussam, W.K., & Sheard, G.J. (2016). Two-dimensional wake dynamics behind cylinders with triangular cross-section under incidence angle variation. *Journal of Fluids and Structures*, 63, 302-324.
- Ozgoren, M., Yagmur, S., Dogan, S., Aksoy, M.H., Canli, E., & Goktepe, I. (2015). Flow characteristics around a vortex flow meter via CFD and PIV methods. In *Proceedings of 10th Pacific Symposium on Flow Visualization and Image Processing*. Naples Italy.
- Prasath, S.G., Sudharsan, M., Kumar, V.V., Diwakar, S.V., Sundararajan, T., & Tiwari, S. (2014). Effects of aspect ratio and orientation on the wake characteristics of low Reynolds number flow over a triangular prism. *Journal of Fluids and Structures*, 46, 59-76.
- Rui, Z., Shang, L., Jianhua, J., Feng, B., & Zhirong, L. (2019). Wake flow dynamic characteristics of triangular prisms. *Fluid Dynamics*, 54, 785-796.
- Sanaei, P., Sun, G., Li, H., Peskin, C.S., & Ristroph, L. (2021). Flight stability of wedges. *Journal of Fluids and Structures*, 101, 103218.
- Seyed-Aghazadeh, B., Carlson, D.W., & Modarres-Sadeghi, Y. (2017). Vortex-induced vibration and galloping of prisms with triangular cross-sections. *Journal of Fluid Mechanics*, 817, 590-618.
- Shih, T.H., Liou, W.W., Shabbir, A., Yang, Z., & Zhu, J. (1994). *A new k-epsilon eddy viscosity model for high Reynolds number turbulent flows: Model development and validation* (No. CMOTT-94-6). National Aeronautics and Space Administration. Cleveland, Ohio, USA.
- Srigrarom, S., & Koh, A.K.G. (2008). Flow field of self-excited rotationally oscillating equilateral triangular cylinder. *Journal of Fluids and Structures*, 24(5), 750-755.
- Tatsuno, M., Takayama, T., Amamoto, H., & Ishi-i, K. (1990). On the stable posture of a triangular or a square cylinder about its central axis in a uniform flow. *Fluid Dynamics Research*, 6(3-4), 201-207.

- Tu, J., Zhou, D., Bao, Y., Han, Z., & Li, R. (2014). Flow characteristics and flow-induced forces of a stationary and rotating triangular cylinder with different incidence angles at low Reynolds numbers. *Journal of Fluids and Structures*, 45, 107-123.
- Versteeg, H.K., & Malalasekara, W. (2010). An introduction to computational fluid dynamics. Pearson Education Ltd., India.
- Wang, H., Liu, Y., Cao, X., & Chen, J. (2019a). Numerical analysis of the effect of the cylinders with different cross sections on the flow field characteristics. In *IOP Conference Series: Earth and Environmental Science* (Vol. 330, No. 2, p. 022056). IOP Publishing. <https://doi.org/10.1088/1755-1315/330/2/022056>.
- Wang, H.K., Yan, Y.H., Chen, C.M., Ji, C.N., & Zhai, Q. (2019b). Numerical investigation on vortex-induced rotations of a triangular cylinder using an immersed boundary method. *China Ocean Engineering*, 33, 723-733.
- Wanik, A., & Schnell, U. (1989). Some remarks on the PISO and SIMPLE algorithms for steady turbulent flow problems. *Computers & Fluids*, 17(4), 555-570.
- Yagmur, S., Dogan, S., Aksoy, M.H., Goktepe, I., & Ozgoren, M. (2017). Comparison of flow characteristics around an equilateral triangular cylinder via PIV and Large Eddy Simulation methods. *Flow Measurement and Instrumentation*, 55, 23-36.
- Zhang, J., Xu, G., Liu, F., Lian, J., & Yan, X. (2016). Experimental investigation on the flow induced vibration of an equilateral triangle prism in water. *Applied Ocean Research*, 61, 92-100.



Original content of this work is copyright © Ram Arti Publishers. Uses under the Creative Commons Attribution 4.0 International (CC BY 4.0) license at <https://creativecommons.org/licenses/by/4.0/>

Publisher's Note- Ram Arti Publishers remains neutral regarding jurisdictional claims in published maps and institutional affiliations.